

FieldFormer: Physics-Informed Transformers for Spatio-Temporal Field Reconstruction from Sparse Sensors

Ankit Bhardwaj¹, Ananth Balashankar², and Lakshminarayanan Subramanian¹

¹Department of Computer Science, New York University, New York, New York

²Google DeepMind, New York, New York

October 7, 2025

Abstract

Spatio-temporal sensor data is often sparse, noisy, and irregular, and existing interpolation or learning methods struggle here because they either ignore governing PDEs or do not scale. We introduce *FieldFormer*, a transformer-based framework for mesh-free spatio-temporal field reconstruction that combines data-driven flexibility with physics-based structure. For each query, FieldFormer gathers a local neighborhood using a learnable velocity-scaled distance metric, enabling anisotropic adaptation to different propagation regimes. Neighborhoods are built efficiently via per-batch offset recomputation, and refined in an expectation-maximization style as the velocity scales evolve. Predictions are made by a local transformer encoder, and physics consistency is enforced through autograd-based PDE residuals and boundary-specific penalties. Across three benchmarks—a scalar anisotropic heat equation, a vector-valued shallow-water system, and a realistic advection-diffusion pollution simulation—FieldFormer consistently outperforms strong baselines by more than 40%. Our results demonstrate that FieldFormer enables accurate (RMSE $< 10^{-2}$), efficient, and physically consistent field reconstruction from sparse (0.4%–2%) and noisy(10%) data.

Code Repository - <https://github.com/ankitbha/fieldformer>

1 Introduction

Many physical systems in environmental science, fluid dynamics, meteorology, and urban infrastructure evolve over space and time, and are naturally described by partial differential equations (PDEs). While such governing laws are well established in controlled settings, real-world observations are often sparse, irregular, and noisy due to limited sensing infrastructure, cost, or sensor failures. This mismatch between continuous dynamics and discrete data poses the challenge of reconstructing the full spatio-temporal field—*field imputation*—from limited observations while remaining consistent with physical principles.

Problem Formulation: Formally, let the latent physical quantity of interest (e.g., temperature, pollutant concentration, fluid velocity) be denoted as a function $u : \mathbb{R}^d \times \mathbb{R} \rightarrow \mathbb{R}^q$, where $u(\mathbf{x}, t)$ represents the value of the field at spatial location $\mathbf{x} \in \mathbb{R}^d$ and time $t \in \mathbb{R}$. In our setting, we are given a sparse set of observations:

$$\mathcal{D} = \{(\mathbf{x}_i, t_i, \mathbf{u}_i)\}_{i=1}^N$$

where $\mathbf{u}_i = \mathbf{u}(\mathbf{x}_i, t_i) + \epsilon_i$ denotes a possibly noisy measurement, and ϵ_i represents measurement noise. The spatial dimension d can be 1, 2, or 3 depending on the application (e.g., 2D urban sensors or 3D climate grids).

The task is to estimate $\mathbf{u}(\mathbf{x}, t)$ at arbitrary *query points* $(\mathbf{x}, t) \in \mathcal{Q}$, where \mathcal{Q} is a continuous or discretized spatio-temporal domain of interest, typically finer or more regular than the observed points \mathcal{D} . Crucially, we assume that the latent field $\mathbf{u}(\mathbf{x}, t)$ satisfies a known or partially known physical law in the form of a partial differential equation

$$\mathcal{F}(\mathbf{x}, t, \mathbf{u}, \nabla \mathbf{u}, \nabla^2 \mathbf{u}, \dots) = 0,$$

where \mathcal{F} is a differential operator involving spatial and temporal derivatives, and ∇, ∇^2 represent first and second-order derivatives with respect to the input coordinates. The key challenge lies in accurately reconstructing $\mathbf{u}(\mathbf{x}, t)$ from irregular and sparse data while respecting the governing PDE, even when initial conditions, boundary conditions, or certain physical parameters (e.g., diffusivity coefficients) or coupled processes are unknown or uncertain.

We further assume that the data exhibits a longitudinal sampling structure: observations are obtained at a relatively small number of spatial locations, each with a dense temporal trace. Formally, for a subset of spatial locations $\{\mathbf{x}_j\}_{j=1}^M$, we observe field values at multiple time steps $\{t_j^{(k)}\}_{k=1}^{T_j}$. We also take the *temporal density* assumption, under which the temporal sampling resolution is fine relative to the timescale of underlying seasonal or periodic dynamics—i.e., dominant temporal trends in $\mathbf{u}(\mathbf{x}, t)$ evolve over coarser timescales than the interval between observations. This setting is common in real-world sensing applications, such as air quality monitoring or traffic flow analysis, where stationary sensors collect temporally dense data despite being sparsely distributed in space.

Classical approaches include interpolation methods such as Kriging or Gaussian process regression (Cressie, 1990), statistical models with spatio-temporal kernels (Wikle et al., 2019; De Luna and Genton, 2005), and physics-based numerical solvers like finite difference and finite element methods (LeVeque, 2007; Hughes, 2003). These methods either scale poorly to large, high-dimensional datasets (e.g., kriging’s cubic time complexity), ignore governing equations in interpolation, or rely on first-principle models that are difficult to tune. Recent machine learning methods—graph neural networks (Wu et al., 2019; Xu et al., 2020), message-passing recurrent networks (Iyer et al., 2022), and transformers (Nie et al., 2024)—have shown strong performance in spatio-temporal forecasting and imputation, but graph-based approaches are tied to discrete graph structures and none of these models explicitly enforce physical structure, often yielding implausible predictions in extrapolative or sparse regimes. Physics-informed neural networks (PINNs) (Raissi et al., 2019) incorporate PDE constraints into training, but they are designed for global coordinate approximations and mesh-based solvers, making them inefficient in longitudinal settings (Krishnapriyan et al., 2021) and ill-suited to localized spatio-temporal structure.

Proposed Solution: We propose *FieldFormer*, a transformer-based framework for spatio-temporal field reconstruction, with the following features:

- A transformer-based architecture that reconstructs fields at any query location using only local neighborhood context, operating directly on sparse point clouds without requiring grids, recurrence, or global positional encodings. Our study emphasizes the more demanding case of two spatial dimensions, extending beyond the predominantly one-dimensional focus of earlier methods.
- A learnable anisotropic velocity-scaled distance metric with scale parameters $\{\gamma_x, \gamma_y, \gamma_t\}$ that adaptively weight spatial and temporal proximity. To avoid expensive kNN searches, neighborhoods are gathered from a pre-computed offset table that is dynamically reweighted as the scales evolve, yielding an expectation–maximization style alternation between neighborhood geometry and model updates.
- A local transformer encoder that represents each neighbor by its relative displacement and observed value, aggregates the resulting patch, and produces query predictions.
- A physics-informed loss that computes PDE residuals directly via autograd with respect to coordinates, and incorporates domain-specific boundary penalties (periodicity for closed domains; sponge/radiation for open domains). Gradient-norm balancing ensures that physics and data terms interact stably during training.
- Comprehensive evaluation on synthetic PDE-driven datasets (heat and shallow-water equations) and semi-synthetic simulations (advection–diffusion for air pollution), where FieldFormer achieves state-of-the-art performance. For example, on the pollution simulation dataset, FieldFormer reduces RMSE to 0.013; outperforming SIREN (0.022), Fourier-MLP (0.3), and SVGP (1.34).

Overall, our framework bridges scientific modeling and machine learning by enabling data-efficient, physically grounded inference on real-world spatio-temporal systems from sparse and irregular observations.

2 Related Work

Spatio-Temporal Imputation from Sparse Observations: Classical methods such as Kriging and Gaussian process regression (Cressie, 1990) rely on spatial stationarity and smoothness priors, but scale

poorly ($O(n^3)$ in n data points) and struggle with irregular sampling or high-dimensional dynamics. Learning-based models have since been proposed to capture complex dependencies: message-passing recurrent neural networks (MPRNNs) (Iyer et al., 2022) address missing values via spatio-temporal dynamics and gating; graph-based approaches like Graph WaveNet (Wu et al., 2019) and ST-Transformer (Xu et al., 2020) use adjacency matrices or learned kernels to encode spatial relations but assume regular layouts; and transformer models such as ImputeFormer (Nie et al., 2024) capture long-range temporal dependencies but treat time as the primary axis. While effective in multivariate time series, none of these methods incorporate prior physical knowledge or enforce PDE consistency, leading to physically implausible interpolations in sparse or extrapolative regimes.

Physics-Informed Neural Networks and Differentiable PDE Solvers: Physics-Informed Neural Networks (PINNs) (Raissi et al., 2019) embed PDE constraints by computing differential operators on network outputs via automatic differentiation and penalizing residuals, enabling both forward and inverse modeling. However, they assume dense, continuous input spaces and typically operate on collocation points over structured grids, leading to degraded performance on sparse or irregular real-world data (Krishnapriyan et al., 2021). In many applications we target—environmental monitoring, traffic modeling, and climate sensing—observations are temporally dense but spatially sparse, with a few fixed-location sensors and wide spatial gaps. Under such longitudinal sampling, global function approximators like PINNs become inefficient or unstable, requiring dense collocation or strong smoothness priors. Other physics-integrated approaches, such as DiffTaichi (Hu et al., 2019) and JAX-FDM (Kochkov et al., 2021), enable differentiable programming over simulation pipelines but still rely on mesh-based discretizations, making them less suitable for data-driven imputation from scattered sensors.

Transformers for Scientific Modeling and Field Inference: The use of Transformer architectures has extended beyond NLP into spatio-temporal domains, and several works have attempted to incorporate physical priors into transformer architectures. TransFlowNet (Wang et al., 2022) introduces physics-constrained loss terms into a transformer model to simulate spatio-temporal flow fields, and Lorsung et al. (2024) integrate attention-based sequence modeling with physics-informed PDE tokens for solving PDEs. These works, however, either assume dense spatial coverage, complete knowledge of underlying physics, or rely on grid-aligned discretizations and global attention, limiting their applicability in sparse or irregular sensor settings and studying real-world systems with externalities.

Hybrid Approaches for Learning with Physical Structure: Recent work has explored combining learning with physical structure without fully modeling the governing PDEs. Neural Operators such as Fourier Neural Operators (FNOs) (Li et al., 2020a) and Graph Neural Operators (Li et al., 2020b) learn mappings between function spaces and approximate PDE solutions, but typically require dense input–output grids and are not suited for scattered data or imputation. Other hybrids, including Physics-Informed Neural Fields (Chu et al., 2022) and Koopman operator methods (Lusch et al., 2018), embed physical constraints or dynamical priors into latent representations, yet generally assume dense trajectories or simulation-generated data and are ill-suited to longitudinal, sparsely observed settings.

3 Method

3.1 FieldFormer Architecture

Local Neighborhood Encoding: Predicting the field value at a query $(\mathbf{x}_q, t_q) \in \mathbb{R}^{d_s} \times \mathbb{R}$ requires local context: PDEs, especially with *local operators*, typically couple a state variable to its spatial and temporal neighbors rather than to the entire domain. To emulate this, FieldFormer extracts a fixed-size local neighborhood from the dataset

$$\mathcal{D} = \{(\mathbf{x}_i, t_i, \mathbf{u}_i)\}_{i=1}^N, \quad \mathbf{u}_i \in \mathbb{R}^q.$$

Neighbors are not chosen by naive Euclidean distance, but by a *velocity-scaled metric* that adapts to anisotropic dynamics:

$$d((\mathbf{x}_q, t_q), (\mathbf{x}_i, t_i)) = \sum_{k=1}^{d_s} \gamma_k^2 (x_{q,k} - x_{i,k})^2 + \gamma_t^2 (t_q - t_i)^2. \quad (1)$$

The learnable parameters $\{\gamma_k\}_{k=1}^{d_s}, \gamma_t$ weight each spatial axis and time relative to one another. They are

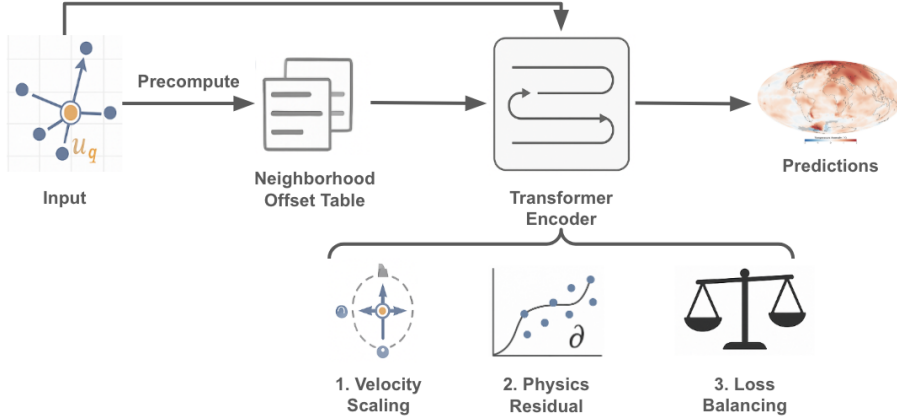


Figure 1: Overview of FieldFormer-Autograd architecture for PDE-conformant field imputation.

parameterized as $\gamma = \exp(\theta)$ to enforce positivity. This scaling allows the model to *discover* the anisotropy of the underlying process: for purely diffusive systems it may amplify temporal proximity, while for advective or wave-like systems it stretches neighborhoods preferentially along flow directions. Thus the model automatically learns whether a time step is "worth" more than a spatial offset.

Each neighbor $(\mathbf{x}_j, t_j, \mathbf{u}_j)$ is encoded relative to the query:

$$\mathbf{v}_j = [\mathbf{x}_j - \mathbf{x}_q, t_j - t_q, \mathbf{u}_j] \in \mathbb{R}^{d_s+1+q},$$

resulting in an input matrix $\mathbf{X}_q \in \mathbb{R}^{n \times (d_s+1+q)}$. This encoding is translation-invariant and emphasizes relative differences, which is crucial when queries are at unseen coordinates.

Efficient Neighbor Search with Offsets: A practical challenge is that neighborhoods must be recomputed for *every* query and for *every* update of the scales γ . A naive kNN search is prohibitively expensive. Instead, we pre-build an *offset table* of integer displacements $(\Delta i, \Delta j, \Delta k)$ in the grid, sorted by the scaled distance (1). Once built, this table can be reused for every query, turning neighborhood selection into a simple index gather rather than a search. This makes neighbor retrieval $\mathcal{O}(1)$ amortized.

The key design here is that neighborhoods adapt as γ evolves: when γ_t is small relative to γ_x , offsets expand farther in time than in space, and vice versa. In practice this leads to an expectation–maximization style loop: (E) compute neighborhoods using current γ , (M) update γ by gradient descent given the neighborhoods. This alternation steadily refines both the geometry and the prediction.

Transformer-Based Local Inference: The neighborhood matrix \mathbf{X}_m is encoded with a transformer encoder with L layers:

$$\mathbf{H}_q = \text{TransformerEncoder}(\mathbf{X}_m) \in \mathbb{R}^{m \times d'},$$

where each row corresponds to a neighbor treated as a token. Because relative deltas already encode spatial and temporal positions, no global positional encoding is required. Mean pooling aggregates neighbor embeddings,

$$\mathbf{h}_q = \frac{1}{m} \sum_{j=1}^m \mathbf{H}_q^{(j)},$$

and a prediction head maps to the output field value:

$$\hat{\mathbf{u}}_q = \text{MLP}(\mathbf{h}_q).$$

This architecture is deliberately local: unlike global attention, its cost is constant per query, and its design aligns with the locality of PDE operators. It is also anisotropy-aware: the same transformer backbone can adapt to diffusion, advection, or wave propagation simply by learning different γ scales.

3.2 Physics-Informed Loss via Autograd

Autograd Residuals: We treat FieldFormer itself as a *coordinate neural field*: given input (\mathbf{x}, t) , its prediction is differentiable w.r.t. the coordinates. Thus derivatives are obtained directly:

$$\nabla u(\mathbf{z}_q) = \frac{\partial u}{\partial \mathbf{z}}(\mathbf{z}_q), \quad \nabla^2 u(\mathbf{z}_q) = \frac{\partial^2 u}{\partial \mathbf{z}^2}(\mathbf{z}_q).$$

For governing PDE

$$\mathcal{F}(\mathbf{x}, t, u, \nabla u, \nabla^2 u, \dots) = 0,$$

the residual at a query is

$$R(\mathbf{z}_q) = \mathcal{F}(\mathbf{z}_q, u(\mathbf{z}_q), \nabla u(\mathbf{z}_q), \nabla^2 u(\mathbf{z}_q)),$$

and the physics loss is the robust Huber penalty

$$\mathcal{L}_{\text{phys}} = \frac{1}{M} \sum_{q=1}^M \text{Huber}(R(\mathbf{z}_q)).$$

This avoids discretization error and automatically respects the anisotropy discovered by γ .

Boundary Conditions: We explicitly handle boundaries: (i) **Periodic domains (Heat, SWE)**: soft equality between opposing faces, optionally including derivatives:

$$\mathcal{L}_{\text{bc}}^{\text{per}} = \|u(x=0, y, t) - u(x=L_x, y, t)\|_2^2.$$

(ii) **Open domains (Pollution)**: a sponge rim loss damps edges, and an Orlanski-style radiation condition enforces

$$u_t + c_{\text{eff}} \partial_n u \approx 0,$$

with c_{eff} estimated from gradients and clamped for stability. Both losses are formulated in normalized coordinates and evaluated via autograd.

Loss Balancing: To prevent one term from dominating, we normalize λ_{pde} so that the gradient norms of data and physics terms are balanced:

$$\lambda_{\text{pde,eff}} = \lambda_{\text{pde}} \cdot \frac{\|\nabla \mathcal{L}_{\text{data}}\|}{\|\nabla \mathcal{L}_{\text{phys}}\|}.$$

Then, the final objective is

$$\mathcal{L}_{\text{total}} = \mathcal{L}_{\text{data}} + \lambda_{\text{pde,eff}} \mathcal{L}_{\text{phys}} + \lambda_{\text{bc}} \mathcal{L}_{\text{bc}}.$$

3.3 Inference and Efficiency

Inference at Arbitrary Locations: Prediction at (\mathbf{x}, t) requires only three steps: 1) Use the pre-computed offset table to gather neighbors under the current scales γ . 2) Encode deltas and neighbor values into \mathbf{X}_m . 3) Forward through the transformer and MLP. Because neighborhoods are constant-sized, complexity per query is $\mathcal{O}(m^2 d)$, independent of total dataset size.

Generalization and Resolution Adaptivity: FieldFormer-Autograd generalizes across resolutions: since inference is purely coordinate-based and local, the model trained at one resolution can be evaluated at another. This enables both upsampling of sparse sensor data into high-resolution fields and coarsening of predictions for downstream models.

Scalability: The offset-based neighbor search reduces lookup cost from $\mathcal{O}(N \log N)$ for kNN(Bentley, 1975) to amortized $\mathcal{O}(1)$. Combined with fixed-size local attention, this yields linear scaling in batch size and constant scaling with grid resolution, in stark contrast to $\mathcal{O}(N^2)$ global transformers.

3.4 Formal Analysis

Expressivity

Definition 3.1 (Finite-order local differential operator). Let $u : \mathbb{R}^{d+1} \rightarrow \mathbb{R}^m$. A differential operator \mathcal{L} is called a *finite-order local operator of order r* if

$$\mathcal{L}u(z) = F(z, \{D^\alpha u(z) : |\alpha| \leq r\}), \quad z \in \mathbb{R}^{d+1},$$

for some continuous function F , where α is a multi-index.

• **Finite-order:** Only derivatives of u up to order $r < \infty$ appear.

• **Local:** $\mathcal{L}u(z)$ depends only on u and its derivatives evaluated at the same point z , not on integrals or values of u away from z .

Examples include the heat operator $\partial_t - \Delta$, the wave operator $\partial_{tt} - c^2 \Delta$, and the advection operator $\partial_t + v \cdot \nabla$. Nonlocal operators such as the fractional Laplacian $(-\Delta)^{\alpha/2}$ are excluded.

Theorem 3.2 (Universal Approximation for Parabolic and Hyperbolic PDEs). *Let $u : \mathbb{R}^d \times \mathbb{R} \rightarrow \mathbb{R}^q$ solve a parabolic or hyperbolic PDE*

$$F(z, u(z), \nabla u(z), \dots, D^r u(z)) = 0, \quad z = (x, t),$$

with a finite-order, local operator. Assume a consistent explicit finite-difference scheme with compact stencil $\mathcal{S} \subset \{-s_{\max}, \dots, s_{\max}\}^d \times \{0, \dots, k\}$ and a CFL-admissible time step Δt . Then for any $\varepsilon > 0$ and compact $K \subset \mathbb{R}^{d+1}$, there exists a FieldFormer with neighborhood size $m \geq |\mathcal{S}|$, hidden width d' , and depth L such that

$$\sup_{z \in K} \|u(z) - \hat{u}(z)\|_2 < \varepsilon.$$

Proof sketch. (1) **Discrete locality.** For an explicit compact-stencil scheme, the update at $(\mathbf{i}, n+1)$ uses only the finite set

$$\mathcal{N}_{\text{FD}}(\mathbf{i}, n+1) := \{(\mathbf{i} + \mathbf{s}, n - \ell) : (\mathbf{s}, \ell) \in \mathcal{S}\},$$

whose spatial radius is $R_x = h \max_{\mathbf{s} \in \mathcal{S}} \|\mathbf{s}\|_2$ and temporal depth $k \Delta t$; hence its size/extent are bounded independently of the grid.

(2) **Finite-dimensional map.** The state at $(\mathbf{i}, n+1)$ is a continuous function $\psi : \mathbb{R}^{|\mathcal{S}|} \rightarrow \mathbb{R}^q$ of the finitely many past neighborhood values.

(3) **Expressivity.** FieldFormer encodes a neighborhood of $m \geq |\mathcal{S}|$ tokens (relative coordinates + values) through a transformer/MLP stack. By universal approximation for MLPs/transformation on compact sets (Hornik, 1991; Yun et al., 2019), taking width d' and depth L large enough yields an arbitrarily accurate approximation to ψ .

(4) **Anisotropy and coverage.** The learnable velocity-scaled metric stretches/compresses the space-time neighborhood so m tokens can cover \mathcal{N}_{FD} .

(5) **Global uniformity.** Since K is compact and covered by finitely many such neighborhoods, uniform approximation on each extends to all of K . \square

Remark 3.3 (Implication: Suitability for Modeling Local Processes). FieldFormer inherits the *locality axiom* of parabolic and hyperbolic PDEs: their discrete updates depend only on a bounded stencil, which FieldFormer can encode via local neighborhoods. Thus, beyond general approximation results, FieldFormer is structurally aligned with the domains of dependence of parabolic and hyperbolic PDEs.

Approximation Error

Assumption 3.4. Setup: Assume the setup of Prop. 3.2 with stencil $\mathcal{S} \subset \{-s_{\max}, \dots, s_{\max}\}^d \times \{0, \dots, k\}$ of size $N := |\mathcal{S}|$. Let the explicit update at $(\mathbf{i}, n+1)$ be

$$u^{n+1}(\mathbf{i}) = \psi(\{u^{n-\ell}(\mathbf{i} + \mathbf{s}) : (\mathbf{s}, \ell) \in \mathcal{S}\}),$$

$$\psi : \mathbb{R}^N \rightarrow \mathbb{R}^q.$$

Assumption 3.5. Sampling Model: Let the stencil factor as

$$\mathcal{S} = \mathcal{S}_x \times \mathcal{T}, \quad \mathcal{S}_x \subset \{-s_{\max}, \dots, s_{\max}\}^d, \\ |\mathcal{S}_x| = N_x, \quad \mathcal{T} = \{0, 1, \dots, k\}.$$

Thus the stencil size is $N = N_x(k+1)$, but coverage is determined entirely by the N_x spatial indices. A sensor placed at spatial offset $s \in \mathcal{S}_x$ provides all $k+1$ time levels.

We randomly place m_x sensors *uniformly without replacement* among the N_x essential spatial locations. FieldFormer then takes all available measurements.

Assumption 3.6. Influence Margin (Average-Case): Let $V \sim \mathcal{D}$ be the random input (stencil values), and $\psi : \mathbb{R}^N \rightarrow \mathbb{R}^q$ the local update map. Index the stencil as $\mathcal{S} = \mathcal{S}_x \times \mathcal{T}$ with $\mathcal{S}_x \subset \{-s_{\max}, \dots, s_{\max}\}^d$ and $\mathcal{T} = \{0, \dots, k\}$, so $N = |\mathcal{S}| = N_x(k+1)$ with $N_x = |\mathcal{S}_x|$.

Assume there exist nonnegative weights $(a_{(s,\ell)})_{(s,\ell) \in \mathcal{S}}$ with $\sum_{(s,\ell) \in \mathcal{S}} a_{(s,\ell)} = 1$ and a constant $c > 0$ such that for every coordinate $(s, \ell) \in \mathcal{S}$ there is a perturbation mechanism $T_{(s,\ell)}$ acting only on (s, ℓ) with

$$\mathbb{E}[\|\psi(V) - \psi(T_{(s,\ell)}V)\|_2] \geq c a_{(s,\ell)}. \quad (2)$$

For longitudinal sampling (a spatial miss hides all time levels), aggregate the weights per spatial offset

$$\bar{a}_s := \sum_{\ell \in \mathcal{T}} a_{(s,\ell)}, \quad s \in \mathcal{S}_x,$$

so that $\bar{a}_s \geq 0$ and $\sum_{s \in \mathcal{S}_x} \bar{a}_s = 1$. For a subset $J \subseteq \mathcal{S}_x$, define its *influence mass* as $A(J) := \sum_{s \in J} \bar{a}_s$.

Theorem 3.7 (Average-Case Lower Bound Under Longitudinal Sampling). *Sample m_x spatial locations uniformly without replacement from \mathcal{S}_x , let $I \subseteq \mathcal{S}_x$ be the sensed set and I^c the missed set. Under equation (2), FieldFormer \hat{u} , using all sensed data, satisfies*

$$\inf_{\hat{u}} \mathbb{E}[\|\hat{u} - u^{n+1}(\mathbf{i})\|_2] \geq c \mathbb{E}[A(I^c)] = c \left(1 - \frac{m_x}{N_x}\right),$$

where the expectation is over the random sampling of I and the data distribution \mathcal{D} .

Proof Sketch. Conditioned on I , all coordinates (s, ℓ) with $s \in I^c$ are unobserved. By linearity of expectation and (2), the Bayes risk is at least $c \sum_{s \in I^c} \bar{a}_s = c A(I^c)$. For uniform m_x -of- N_x sampling, $\mathbb{E}[A(I^c)] = \sum_{s \in \mathcal{S}_x} \bar{a}_s \Pr(s \notin I) = (1 - m_x/N_x) \sum_s \bar{a}_s = 1 - m_x/N_x$. Averaging over different points gives this claim. \square

Remark 3.8 (Implication: Effect of Stencil Size on Miss-Coverage Error). The miss-coverage term depends only on the number of essential spatial offsets N_x , since all $k+1$ time levels are obtained once a spatial site is sensed. With error (E) as

$$E(N_x) = c \left(1 - \frac{m_x}{N_x}\right), \quad \frac{dE}{dN_x} = -c \frac{m_x}{N_x^2} < 0,$$

the bound decreases as N_x decreases: fewer essential sites are easier to cover with a fixed m_x . Parabolic PDEs like the heat equation involve second-order spatial derivatives, so standard discretizations require broader stencils (e.g. Laplacian neighbors). In contrast, hyperbolic PDEs like the shallow water equations involve first-order flux derivatives, which can be captured with only nearest neighbors. Hence N_x is typically larger for heat than for SWE, explaining why the latter shows lower miss-coverage error in the empirical results (Table 1).

4 Evaluation

4.1 Baselines and Metrics

Gaussian Processes: Gaussian Processes (also called Kriging) (Cressie, 1990) with separable spatio-temporal kernels represent the classical gold standard for interpolation. They can be queried at arbitrary

spatio-temporal points (x, y, t) , making them a direct comparator. Their main limitation is computational scalability, but they provide a principled baseline grounded in geostatistics. To ensure scalability, we employ stochastic variational Gaussian processes (SVGPs) (Hensman et al., 2013), which use a variational formulation with inducing points to handle large training sets while preserving predictive flexibility. We carefully tune the number of inducing points and optimize kernel hyperparameters to provide a competitive GP baseline.

Neural Fields: Coordinate-based neural networks (MLPs with positional encodings) define a continuous surrogate model $f(x, y, t)$ that can be evaluated at any query location. We select two widely adopted architectures that represent complementary design choices: (i) Fourier-MLPs (Tancik et al., 2020), which use high-dimensional sinusoidal encodings of inputs to capture sharp variations and fine-scale structures; and (ii) SIRENs (Sitzmann et al., 2020), which employ sinusoidal activations throughout the network to directly model high-frequency spatio-temporal signals. Both models are trained with standard weight initialization schemes proposed in their original works to ensure stable convergence and faithful reproduction of sharp PDE-driven dynamics. We also include physics-regularized loss (PINNs) (Raissi et al., 2019) during training in these baselines.

Baseline Selection: These baselines were chosen because they cover the three main paradigms for mesh-free spatio-temporal field reconstruction: (i) probabilistic inference with GPs, (ii) coordinate-based neural fields with frequency encodings or sinusoidal activations, and (iii) physics-informed neural networks. Each baseline was implemented following the best practices in the original papers, with architectures, activation functions, encoding schemes, and optimization strategies matched to their canonical implementations. Together, they provide strong and diverse comparators that capture smooth interpolation (SVGP), high-frequency reconstruction (Fourier-MLP, SIREN), and physics-informed regularization (PINN). Grid-based operator models (e.g., FNO(Li et al., 2020a), UNO(Rahman et al., 2022), U-Net(Ronneberger et al., 2015)) and graph-based spatio-temporal models (e.g., Graph WaveNet(Wu et al., 2019), DCRNN(Li et al., 2017)) are not included as direct baselines. These methods are tied to fixed discretizations: operator models require full grid inputs and outputs, while graph models assume a fixed set of sensor nodes. As a result, they cannot natively support mesh-free queries at arbitrary coordinates, nor extrapolate beyond the training grid or sensor graph. While effective in dense simulation or fixed-sensor settings, they are fundamentally mismatched to the sparse sensing imputation problem that FieldFormer targets.

Metrics: We report RMSE and MAE on sensor test sets and full fields, along with relative physics residuals normalized by derivative scales. These residuals serve only as a sanity check of physical consistency, since overly smooth predictions can yield deceptively low values without accurate or plausible reconstructions.

4.2 Evaluation Settings and Results

Periodic Heat Equation (2D): We first evaluate on a controlled synthetic setting governed by the anisotropic two-dimensional heat equation with periodic boundary conditions,

$$u_t = \alpha_x u_{xx} + \alpha_y u_{yy} + f(x, y, t),$$

where the forcing term is a smooth sinusoidal function of space and time. The domain is discretized on a 64×64 spatial grid with 10,000 time steps, and stability is enforced via the CFL condition. A smooth sinusoidal initial condition is evolved forward using explicit finite differences with periodic wrapping. From the resulting full field, we sample 20 sensor locations uniformly at random and extract both clean and noisy time series. Noise is scaled relative to the maximum magnitude, ensuring realistic observation corruption. The dataset is stored in compressed format with complete metadata (grid, parameters, sensor indices) for reproducibility. This benchmark provides a clean, scalar yet anisotropic setting where all physical parameters and boundary behavior are fully known.

Table 1, part 1 reports reconstruction and physics error metrics on this benchmark. FieldFormer achieves low reconstruction error while maintaining moderate PDE residuals, showing that it can exploit the anisotropic structure captured by the learnable velocity scales. In contrast, SIREN and Fourier-MLP baselines incur an order-of-magnitude higher RMSE, reflecting their difficulty in capturing smooth yet anisotropic diffusion. SVGP attains the lowest RMSE numerically but exhibits very large raw PDE residuals, indicating oversmoothing that fits the sensors but violates the dynamics. Relative residuals highlight this contrast more fairly: FieldFormer reduces normalized errors below both SIREN and SVGP, balancing fidelity to data

Table 1: Performance across all datasets. Metrics are reported with multipliers factored out for clarity. We report RMSE and MAE on the sensor test set (with bootstrap mean \pm std), full-field reconstruction errors, and relative PDE residual errors (test and full) where applicable.

Dataset/Metric	FieldFormer	SIREN	Fourier-MLP	SVGP	
Heat	Test RMSE (bootstrap) ($\times 10^{-2}$)	1.133 ± 0.00063	7.983 ± 0.0067	12.59 ± 0.0161	0.592 ± 0.00034
	Test MAE (bootstrap) ($\times 10^{-3}$)	7.715 ± 0.0028	56.47 ± 0.025	25.32 ± 0.036	3.627 ± 0.0016
	Full-field RMSE ($\times 10^{-2}$)	<u>1.133</u>	7.978	12.57	0.592
	Full-field MAE ($\times 10^{-3}$)	<u>7.714</u>	56.45	25.30	3.628
	Rel. Physics RMSE (test)	0.660	0.638	0.246	0.674
	Rel. Physics MAE (test)	0.603	0.538	0.071	0.575
	Rel. Physics RMSE (full)	0.658	0.639	0.240	0.674
	Rel. Physics MAE (full)	0.600	0.539	0.068	0.575
SWE	Test RMSE (bootstrap) ($\times 10^{-3}$)	1.113 ± 0.00153	70.46 ± 0.0179	63.76 ± 0.0104	180.1 ± 0.0378
	Test MAE (bootstrap) ($\times 10^{-4}$)	8.151 ± 0.0242	516.5 ± 1.14	468.6 ± 0.558	1312 ± 3.77
	Full-field RMSE ($\times 10^{-3}$)	1.112	70.47	63.77	180.0
	Full-field MAE ($\times 10^{-4}$)	8.150	516.6	468.6	1311
	Rel. Physics RMSE (test)	0.782	0.169	0.190	0.932
	Rel. Physics MAE (test)	0.716	0.0672	0.0753	0.918
	Rel. Physics RMSE (full)	0.781	0.167	0.184	0.932
	Rel. Physics MAE (full)	0.716	0.0662	0.0732	0.917
Pollution	Test RMSE (bootstrap) ($\times 10^{-2}$)	1.310 ± 0.00124	2.188 ± 0.0108	30.16 ± 0.141	134.1 ± 0.153
	Test MAE (bootstrap) ($\times 10^{-3}$)	4.808 ± 0.00723	5.510 ± 0.0141	60.92 ± 0.148	1069 ± 0.466
	Full-field RMSE ($\times 10^{-2}$)	1.319	2.208	30.21	134.3
	Full-field MAE ($\times 10^{-3}$)	4.822	5.530	60.86	1070

with fidelity to physics. These results confirm that in a fully specified anisotropic PDE setting, FieldFormer provides accurate reconstructions that remain more physically consistent than strong neural field or GP baselines.

Periodic Shallow Water Equations (2D): We next evaluate on a more complex synthetic setting governed by the linearized two-dimensional shallow water equations with periodic boundary conditions,

$$\eta_t + H(u_x + v_y) = 0, \quad u_t + g\eta_x = 0, \quad v_t + g\eta_y = 0,$$

which describe the propagation of free-surface *gravity waves*. Unlike the purely diffusive heat equation, this system is hyperbolic and supports oscillatory, wave-like solutions with characteristic speed $c = \sqrt{gH}$. A Gaussian bump in surface height is used as the initial condition, generating outward-traveling gravity waves. The domain is discretized on a 64×64 spatial grid with 10,000 time steps, and numerical stability is enforced through a conservative Courant–Friedrichs–Lewy (CFL) condition for the forward–backward time stepping scheme. From the resulting fields (η, u, v) , we sample 20 sensor locations to obtain clean and noisy time series. This benchmark is more challenging than the heat equation, involving coupled height–velocity evolution, oscillatory rather than diffusive dynamics, and stricter stability constraints. As an isotropic *vector-valued* system with three interdependent quantities, it provides a stringent test of consistent wave propagation and physical fidelity.

Table 1, part 2 presents results on this benchmark. FieldFormer achieves the lowest reconstruction error by more than an order of magnitude compared to neural field baselines. SIREN and Fourier-MLP fail to capture long-range oscillations and incur significantly higher errors, while SVGP produces the largest RMSE. Relative residual metrics reveal that FieldFormer maintains more balanced consistency with the governing PDE than SIREN or Fourier-MLP, while still far outperforming SVGP in reconstruction accuracy. These results highlight the difficulty of isotropic, vector-valued PDE systems and confirm that FieldFormer is able to reconcile multi-variable coupling with accurate field reconstruction.

Real-World Advection–Diffusion Pollution Simulation: To evaluate our methods on a realistic transport–diffusion regime, we simulate pollutant dispersion over New Delhi using the two-dimensional advection–diffusion equation,

$$u_t + \mathbf{v}(t) \cdot \nabla u = \kappa \nabla^2 u + S(x, y),$$

on a normalized $[0, 1] \times [0, 1]$ domain corresponding to the city’s geographic extent. The initial concentration field is constructed from the 32 regulatory monitoring stations(CPCB, 2025) on June 1, 2018, the first day of monsoon, interpolated onto the model grid using Universal Kriging. The source field combines emissions from brick kilns and industries sourced from Guttikunda and Calori (2013), population density from Columbia University (2018), and traffic intensity layers from Google Maps, cropped to the simulation window and normalized. Advection is driven by a synthetic *monsoon-mode wind* oriented toward the northeast, scaled from a 3.5 m/s base flow, based on averaged wind-speeds data from NCEP (2000), and time-compressed so that five simulation seconds correspond to one real day. To capture realistic variability, the wind includes diurnal strengthening and weakening, a small directional wobble, and autoregressive (AR(1)) stochastic gusts with multi-hour correlation times. Horizontal turbulent mixing is represented by a diffusivity chosen to yield an advection-dominated Péclet number at the city scale. Open lateral boundaries are treated with Orlanski-type radiation conditions supplemented by a sponge layer to minimize reflections.

We discretize the PDE with finite differences—upwind for advection, central for diffusion—and advance with a two-stage Heun (RK2) scheme. The simulation produces full spatio-temporal concentration fields as well as time series at sensor gridpoints, to which observation noise is added to reflect sensor variability. This benchmark captures the key challenges of urban air-quality modeling: heterogeneous sources, diurnally varying winds with stochastic gusts, and sparse, noisy sensor measurements. More importantly, it represents a *partial-physics setting*: while the governing PDE is known in form, the advecting wind field is uncertain and highly variable, meaning that enforcing the equation itself is not feasible. Instead, only partial constraints such as open-boundary conditions can be reliably applied, making this benchmark more reflective of real-world scenarios than the fully specified synthetic cases.

Table 1, part 3 reports results on this partial-physics benchmark. FieldFormer achieves the lowest reconstruction errors across both RMSE and MAE, substantially outperforming the baselines. SVGP severely underfits in this complex, heterogeneous regime, producing errors more than a hundred times larger than FieldFormer. These results highlight that in realistic advection–diffusion settings with unknown winds and only boundary physics available, FieldFormer is able to reconcile partial physical structure with data-driven reconstruction, providing both robustness and accuracy in conditions where full physics-based enforcement is difficult.

5 Discussion and Conclusion

FieldFormer offers a scalable and physically grounded framework for spatio-temporal field reconstruction, achieving strong performance across diverse benchmarks and surpassing both physics-regularized data-driven and classical baselines in accuracy. By combining local transformer inference with learnable anisotropic neighborhoods and differentiable physics regularization, the model enables mesh-free reconstruction on sparse, irregular sensor networks. While promising, some challenges remain: defining velocity-scaled local neighborhoods may be less effective in highly nonlocal or chaotic systems; autograd-based physics losses can be sensitive near sharp gradients or discontinuities; and the approach assumes that governing PDEs are at least partially known, whereas real-world dynamics may involve hidden processes. Moreover, predictive quality may diminish under extreme sparsity or sensor drift. Addressing these limitations through uncertainty-aware inference, robust physics integration, and hybrid discovery of unknown dynamics represents an important direction for future work.

6 Acknowledgements

Ankit Bhardwaj and Lakshminarayanan Subramanian were supported by the NSF Grant (Award Number 2335773) titled ”EAGER: Scalable Climate Modeling using Message-Passing Recurrent Neural Networks”. Lakshminarayanan Subramanian was also funded in part by the NSF Grant (award number OAC-2004572) titled ”A Data-informed Framework for the Representation of Sub-grid Scale Gravity Waves to Improve Climate Prediction”.

References

Jon Louis Bentley. Multidimensional binary search trees used for associative searching. *Communications of the ACM*, 18(9):509–517, 1975.

Mengyu Chu, Lingjie Liu, Quan Zheng, Erik Franz, Hans-Peter Seidel, Christian Theobalt, and Rhaleb Zayer. Physics informed neural fields for smoke reconstruction with sparse data. *ACM Transactions on Graphics (ToG)*, 41(4):1–14, 2022.

Center for International Earth Science Information Network . CIESIN Columbia University. Gridded population of the world, version 4 (gpwv4): Population density, revision 11, 20230129 2018. URL <https://doi.org/10.7927/H49C6VHW>.

CPCB. Cpcb data portal. <https://app.cpcbccr.com/CCR/#/CAAQM-Dashboard-all/CAAQM-Landing/CAAQM-Comparison-Data>, 2025.

Noel Cressie. The origins of kriging. *Mathematical geology*, 22:239–252, 1990.

Xavier De Luna and Marc G Genton. Predictive spatio-temporal models for spatially sparse environmental data. *Statistica Sinica*, pages 547–568, 2005.

Sarath K. Guttikunda and Giuseppe Calori. A gis based emissions inventory at 1 km × 1 km spatial resolution for air pollution analysis in delhi, india. *Atmospheric Environment*, 67:101–111, 2013. ISSN 1352-2310. doi: <https://doi.org/10.1016/j.atmosenv.2012.10.040>. URL <https://www.sciencedirect.com/science/article/pii/S1352231012010229>.

James Hensman, Nicolo Fusi, and Neil D Lawrence. Gaussian processes for big data. *arXiv preprint arXiv:1309.6835*, 2013.

Kurt Hornik. Approximation capabilities of multilayer feedforward networks. *Neural networks*, 4(2):251–257, 1991.

Yuanming Hu, Luke Anderson, Tzu-Mao Li, Qi Sun, Nathan Carr, Jonathan Ragan-Kelley, and Frédo Durand. DiffTaichi: Differentiable programming for physical simulation. *arXiv preprint arXiv:1910.00935*, 2019.

Thomas JR Hughes. *The finite element method: linear static and dynamic finite element analysis*. Courier Corporation, 2003.

Shiva R Iyer, Ananth Balashankar, William H Aeberhard, Sujoy Bhattacharyya, Giuditta Rusconi, Lejo Jose, Nita Soans, Anant Sudarshan, Rohini Pande, and Lakshminarayanan Subramanian. Modeling fine-grained spatio-temporal pollution maps with low-cost sensors. *npj Climate and Atmospheric Science*, 5(1):76, 2022.

Dmitrii Kochkov, Jamie A Smith, Ayya Alieva, Qing Wang, Michael P Brenner, and Stephan Hoyer. Machine learning-accelerated computational fluid dynamics. *Proceedings of the National Academy of Sciences*, 118(21):e2101784118, 2021.

Aditi Krishnapriyan, Amir Gholami, Shandian Zhe, Robert Kirby, and Michael W Mahoney. Characterizing possible failure modes in physics-informed neural networks. *Advances in neural information processing systems*, 34:26548–26560, 2021.

Randall J LeVeque. Finite difference methods for ordinary and partial differential equations: steady-state and time-dependent problems, 2007.

Yaguang Li, Rose Yu, Cyrus Shahabi, and Yan Liu. Diffusion convolutional recurrent neural network: Data-driven traffic forecasting. *arXiv preprint arXiv:1707.01926*, 2017.

Zongyi Li, Nikola Kovachki, Kamayr Azizzadenesheli, Burigede Liu, Kaushik Bhattacharya, Andrew Stuart, and Anima Anandkumar. Fourier neural operator for parametric partial differential equations. *arXiv preprint arXiv:2010.08895*, 2020a.

Zongyi Li, Nikola Kovachki, Kamyar Azizzadenesheli, Burigede Liu, Kaushik Bhattacharya, Andrew Stuart, and Anima Anandkumar. Neural operator: Graph kernel network for partial differential equations. *arXiv preprint arXiv:2003.03485*, 2020b.

Cooper Lorsung, Zijie Li, and Amir Barati Farimani. Physics informed token transformer for solving partial differential equations. *Machine Learning: Science and Technology*, 5(1):015032, 2024.

Bethany Lusch, J Nathan Kutz, and Steven L Brunton. Deep learning for universal linear embeddings of nonlinear dynamics. *Nature communications*, 9(1):4950, 2018.

NCEP. Ncep fnl operational model global tropospheric analyses, continuing from july 1999, 2000. URL <https://doi.org/10.5065/D6M043C6>.

Tong Nie, Guoyang Qin, Wei Ma, Yuwen Mei, and Jian Sun. Imputeformer: Low rankness-induced transformers for generalizable spatiotemporal imputation. In *Proceedings of the 30th ACM SIGKDD Conference on Knowledge Discovery and Data Mining*, pages 2260–2271, 2024.

Md Ashiqur Rahman, Zachary E Ross, and Kamyar Azizzadenesheli. U-no: U-shaped neural operators. *arXiv preprint arXiv:2204.11127*, 2022.

Maziar Raissi, Paris Perdikaris, and George E Karniadakis. Physics-informed neural networks: A deep learning framework for solving forward and inverse problems involving nonlinear partial differential equations. *Journal of Computational physics*, 378:686–707, 2019.

Olaf Ronneberger, Philipp Fischer, and Thomas Brox. U-net: Convolutional networks for biomedical image segmentation. In *International Conference on Medical image computing and computer-assisted intervention*, pages 234–241. Springer, 2015.

Vincent Sitzmann, Julien Martel, Alexander Bergman, David Lindell, and Gordon Wetzstein. Implicit neural representations with periodic activation functions. *Advances in neural information processing systems*, 33: 7462–7473, 2020.

Matthew Tancik, Pratul Srinivasan, Ben Mildenhall, Sara Fridovich-Keil, Nithin Raghavan, Utkarsh Singhal, Ravi Ramamoorthi, Jonathan Barron, and Ren Ng. Fourier features let networks learn high frequency functions in low dimensional domains. *Advances in neural information processing systems*, 33:7537–7547, 2020.

Xinjie Wang, Siyuan Zhu, Yundong Guo, Peng Han, Yucheng Wang, Zhiqiang Wei, and Xiaogang Jin. Transflownet: A physics-constrained transformer framework for spatio-temporal super-resolution of flow simulations. *Journal of Computational Science*, 65:101906, 2022.

Christopher K Wikle, Andrew Zammit-Mangion, and Noel Cressie. *Spatio-temporal statistics with R*. Chapman and Hall/CRC, 2019.

Zonghan Wu, Shirui Pan, Guodong Long, Jing Jiang, and Chengqi Zhang. Graph wavenet for deep spatial-temporal graph modeling. *arXiv preprint arXiv:1906.00121*, 2019.

Mingxing Xu, Wenrui Dai, Chunmiao Liu, Xing Gao, Weiyao Lin, Guo-Jun Qi, and Hongkai Xiong. Spatial-temporal transformer networks for traffic flow forecasting. *arXiv preprint arXiv:2001.02908*, 2020.

Chulhee Yun, Srinadh Bhojanapalli, Ankit Singh Rawat, Sashank J Reddi, and Sanjiv Kumar. Are transformers universal approximators of sequence-to-sequence functions? *arXiv preprint arXiv:1912.10077*, 2019.